

## CROSS SECTION FOR THE ASTROPHYSICAL $^{14}\text{C}(n, \gamma)^{15}\text{C}$ REACTION VIA THE INVERSE REACTION

Á. HORVÁTH,<sup>1,2</sup> J. WEINER,<sup>1,3</sup> A. GALONSKY,<sup>1,3</sup> F. DEÁK,<sup>2</sup> Y. HIGURASHI,<sup>4</sup> K. IEKI,<sup>4</sup> Y. IWATA,<sup>4</sup>  
 Á. KISS,<sup>2</sup> J. J. KOLATA,<sup>5</sup> Z. SERES,<sup>6</sup> J. VON SCHWARZENBERG,<sup>5</sup> H. SCHELIN,<sup>7</sup> S. TAKEUCHI,<sup>4</sup>  
 S. TYPPEL,<sup>1</sup> AND R. E. WARNER<sup>8</sup>

Received 2001 July 9; accepted 2002 January 18

### ABSTRACT

The  $^{14}\text{C}(n, \gamma)^{15}\text{C}$  reaction is important in neutron-induced CNO cycles of stellar evolution phases beyond the main sequence. The chain of reactions in primordial nucleosynthesis in the neutron-rich environment of an inhomogeneous big bang also involves the  $^{14}\text{C}(n, \gamma)^{15}\text{C}$  reaction. We have used a beam of  $^{15}\text{C}$  ions at  $E/A = 35$  MeV to measure cross sections for  $^{15}\text{C}$  breakup on targets of C, Al, Zn, Sn, and Pb. The Coulomb part of the breakup cross section was determined as a function of decay energy. By the principle of detailed balance, the neutron capture cross section was then determined as a function of neutron energy. This excitation function rises with energy to  $7 \mu\text{barns}$  at 300 keV and falls to  $2 \mu\text{barns}$  at 1.2 MeV. In the stellar-burning region, our cross section exceeds a previous measurement by a factor of 3. Neither the shape nor the magnitude of the excitation function agrees with those of theoretical calculations based on the direct capture model. The reaction rate is calculated reliably up to  $\sim T_9 = 5$ . In the temperature range of inhomogeneous big bang models, our rate exceeds the rate of the  $^{14}\text{C}(p, \gamma)^{15}\text{N}$  reaction for  $T_9 < 1.2$ .

*Subject headings:* early universe — nuclear reactions, nucleosynthesis, abundances

### 1. INTRODUCTION

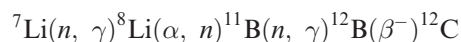
Neutrons produced in the burning zone of 1–3  $M_\odot$  asymptotic giant branch (AGB) stars by the  $^{13}\text{C}(\alpha, n)$  reaction can drive a CNO cycle in which an  $\alpha$ -particle is synthesized from four neutrons (Wiescher, Görres, & Schatz 1999):



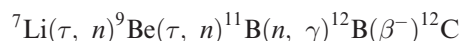
In this cycle, the slowest and therefore controlling reaction is the  $^{14}\text{C}(n, \gamma)^{15}\text{C}$  reaction. The importance of these neutron-induced cycles cannot be known until the cross section for this capture reaction is measured over a range of energies.

Another need for these measurements is related to the inhomogeneous big bang model. In the framework of this model of the early universe, certain scenarios are discussed that generate matter density fluctuations that survive

throughout the era of primordial nucleosynthesis. Such density fluctuations will result in neutron-rich and proton-rich zones as a result of the difference between neutron and proton diffusion times. Inhomogeneous big bang nucleosynthesis (BBN) may resolve the conflict between observations of primordial deuterium and helium, the deuterium abundance requiring a higher baryon density than the helium (Kainulainen, Kurki-Suonio, & Sihvola 1999). The baryon density required by BOOMERANG (de Bernardis et al. 2000) and Maxima-1 (Hanany et al. 2000) observations of the cosmic microwave background exceeds that allowed by standard BBN theory and observed primordial light element abundances. It has recently been shown (Kainulainen & Sihvola 2001), however, that inhomogeneous BBN theory can be consistent with deuterium and helium abundances, although it predicts twice as much  $^7\text{Li}$  as is on the Spite plateau. A similar result has been found by Jedamzik & Rehm (2001), who also find that inhomogeneous BBN underpredicts the abundances of  $^6\text{Li}$ ,  $^9\text{Be}$ , and  $^{11}\text{B}$ . The choice between standard and inhomogeneous BBN is not yet clear. In the neutron-rich zones, the standard route of nucleosynthesis may not be followed, and the model predicts an observable amount of  $A > 12$  elements (Orito et al. 1997) and may even allow a higher baryon density than the standard model (Rauscher et al. 1994). Under this special circumstance, mostly neutron captures and beta decays can create the heavier nuclei. Once  $^7\text{Li}$  is synthesized, two possible chains are proposed to bridge the  $A = 8$  gap in neutron-rich zones:



(Malaney & Fowler 1988) and



(Kajino, Mathews, & Fuller 1990). After  $^{12}\text{C}$  is produced, successive neutron captures lead to  $^{14}\text{C}$ . Since the half-life of  $^{14}\text{C}$  is much larger than the timescale of this nucleosynthesis,

<sup>1</sup> National Superconducting Cyclotron Laboratory, East Lansing, MI 48824-1321; akos@ludens.elte.hu, johnw@ssl.berkeley.edu, galonsky@nscl.msu.edu, typel@nscl.msu.edu.

<sup>2</sup> Department of Atomic Physics, Eötvös Loránd University, Pázmány Peter Sétány 1/A, H-1117 Budapest, Hungary; deak@ludens.elte.hu, kissadam@ludens.elte.hu.

<sup>3</sup> Department of Physics and Astronomy, Michigan State University, East Lansing, MI 48824-1321.

<sup>4</sup> Department of Physics, Rikkyo University, 3 Nishi-Ikebukuro, Toshima, Tokyo 171-8501, Japan; ieki@rikkyo.ac.jp, y\_iwata@nirs.go.jp, takeuchi@se.rikkyo.ac.jp.

<sup>5</sup> Department of Physics, University of Notre Dame, Notre Dame, IN 46556; kolata.1@nd.edu, schwarzenberg@nd.edu.

<sup>6</sup> KFKI Research Institute for Particle and Nuclear Physics, Konkoly-Thege út 29-33, P.O. Box 49, H-1525 Budapest 114, Hungary; seres@rmki.kfki.hu

<sup>7</sup> Centro Federal de Educação Tecnológica do Paraná, Avenue Sete de Setembro 3165 80230-901, Curitiba, Paraná, Brazil; schelin@cpgei.cetep.br.

<sup>8</sup> Department of Physics, Oberlin College, Oberlin, OH 44074; Robert.Warner@oberlin.edu.

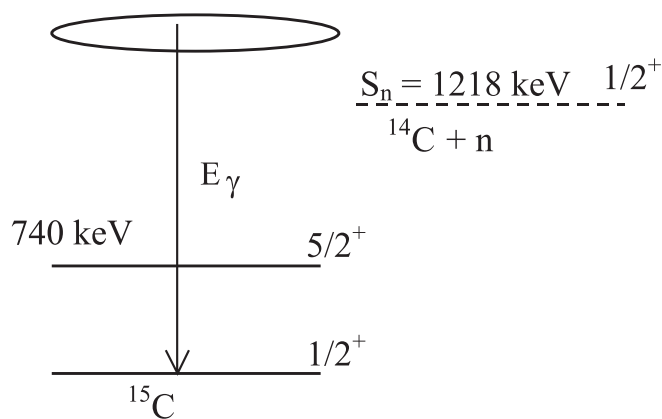
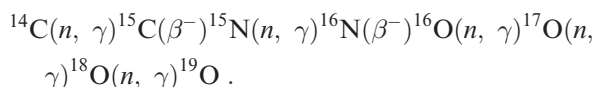


FIG. 1.—Relevant nuclear states and energetics. In the  $(n, \gamma)$  reaction, a photon with energy  $E_\gamma = S_n + E_{\text{CM}}$  is emitted;  $E_{\text{CM}}$  is the  $^{14}\text{C} + n$  energy in its center of mass (CM) system. In the inverse reaction, the  $\gamma$ -ray dissociates  $^{15}\text{C}$  into  $^{14}\text{C} + n$  with decay energy  $E_d = E_{\text{CM}} = E_\gamma - S_n$ .

it is a potential seed nucleus to produce heavier elements via neutron captures and beta decays along the reaction chains proposed by Kajino et al. (1990):



Then,  $A > 20$  neon isotopes can be reached in a series of neutron captures and beta decays. Beside this series,  $^{14}\text{C}$  can be a starting point of different reaction chains in which the first reaction is, instead of neutron capture, radiative capture of  $\alpha$ -particles or protons. Wiescher, Görres, & Thielemann (1990) have predicted that the dominant reaction among these three is neutron capture. Our experiment measured the cross section for that capture up to  $E_n \sim 1$  MeV.

As Figure 1 indicates, the last neutron in  $^{15}\text{C}$  is bound by 1218 keV, and there is a bound excited state at 740 keV. The next state, at 3.1 MeV, being only 42 keV wide, is too high to affect neutron capture for  $E_n$  below  $\sim 1$  MeV. The main reaction mechanism in that region is thought to be direct neutron capture to the  $1/2^+$  ground state and to the  $5/2^+$  first excited state.

The total angular momentum and parity of the system of  $^{14}\text{C}$  and an s-wave neutron is  $1/2^+$ . From such a continuum state, there is no E1 transition to either the ground state or the first excited state of  $^{15}\text{C}$ . An s-wave capture can be followed only by a weaker transition, E2 (Wiescher et al. 1990) or M1 (Kajino et al. 1990). Indeed, in 1950 the thermal capture cross section was found to be less than  $1 \mu\text{barn}$  (Yaffe & Stevens 1950) and, in view of the  $1/v$  rule, its s-wave part would be even smaller at higher energies. However, a p-wave neutron and  $^{14}\text{C}$  form  $1/2^-$  and  $3/2^-$  states, which allow E1 transitions to both the ground and excited states. p-wave capture results in a cross section that increases initially with energy as  $E^{1/2}$ . Using a neutron source having an energy distribution that approximated a Maxwell-Boltzmann distribution with  $kT = 23$  keV, Beer et al. (1992) measured the cross section for the  $^{14}\text{C}(n, \gamma)^{15}\text{C}$  reaction and found that it was  $1.1 \pm 0.28 \mu\text{barns}$  at  $E_n = 23$  keV. Our aim was to determine the excitation function for the capture to as high an energy as possible and, thereby, to extend our knowledge of the reaction rate to higher temperatures.

### 1.1. Concept of the Inverse Reaction Measurement

The main idea of our experiment was to measure the cross section for the inverse reaction—photodisintegration—and apply the principle of detailed balance to determine the radiative neutron capture cross section. Since it is not possible to produce a  $^{15}\text{C}$  target,  $^{15}\text{C}$  becomes the projectile, and the virtual photons near a high- $Z$  nucleus become the targets. The features of the virtual photons are well described theoretically (Bertulani & Baur 1988; Alder & Winther 1966). In general, this inverse technique allows  $(n, \gamma)$  cross sections of astrophysical interest to be determined for nuclei far from the valley of stability. An advantage of using the inverse direction is that, for  $E_n$  greater than a few keV, phase space factors favor the inverse breakup cross section by 1–2 orders of magnitude in comparison to the capture reaction. This enabled us to determine microbarns of  $(n, \gamma)$  cross section by measuring millibarns of the inverse. Another advantage of using the inverse reaction is that we avoid dealing with a dangerous and expensive  $^{14}\text{C}$  target. There are two disadvantages: (1) the need to measure the final state kinematics of each event in order to determine the energy of the photon absorbed, which requires a  $^{14}\text{C} + n$  coincidence measurement, and (2) the need to extract the Coulomb part from the measured Coulomb+nuclear dissociation.

If neutron capture were to go predominantly to an excited state, measuring the inverse cross section would not be relevant because the target nuclei for a photodisintegration experiment are always in the ground state, not the excited state. Although  $^{15}\text{C}$  has a  $5/2^+$  bound excited state at 0.74 MeV, as we show in § 3.3, capture into this state is much smaller than into the ground state. Hence,  $\sigma_{n,\gamma}$  can give us

## 2. EXPERIMENTAL PROCEDURE

### 2.1. Description of the Experiment

The experiment was done at the National Superconducting Cyclotron Laboratory at Michigan State University. Ions of  $^{18}\text{O}^{6+}$  with  $E/A = 80$  MeV from the K1200 cyclotron produced a variety of nuclear species by projectile-like fragmentation in a Be target. The resulting  $^{15}\text{C}$  nuclei at  $E/A = 35$  MeV were selected in the A1200 magnetic fragment separation system (Sherrill et al. 1991) operated with a 1% momentum slit and transported to our experiment station about 40 m away. During the experiment, the  $^{15}\text{C}$  beam intensity averaged  $\sim 20,000 \text{ s}^{-1}$ , and the impurities, mostly Be isotopes, were less than 0.1%.

Although the primary target was Pb, we used four additional targets of lower  $Z$  to enable us to subtract out the nuclear component of the dissociation of  $^{15}\text{C}$  into  $^{14}\text{C} + n$ . The targets were C, Al, Zn, Sn, and Pb with thickness equal to 120, 123, 158, 204, and 283  $\text{mg cm}^{-2}$ , respectively. The layout of the experiment is presented in Figure 2. Unreacted  $^{15}\text{C}$  beam particles and  $^{14}\text{C}$  reaction fragments gave  $\Delta E$  signals in one of two 250  $\mu\text{m}$  thick double-sided silicon strip detectors ( $16 \times 16$ , 3 mm wide electrode strips) placed 15.2 cm downstream at the entrance to the magnetic field. Charged particles were deflected by  $\sim 20^\circ$  in the vertical field of the magnet to an array of fragment  $E$  detectors. The array consists of 16 vertical bars of BC 408 plastic scintillator with photomultiplier tubes attached at both ends (Kruse et al. 2002). The bars, being 2 cm thick, stopped all of the carbon nuclei. By calibrating with carbon isotopes of known ener-

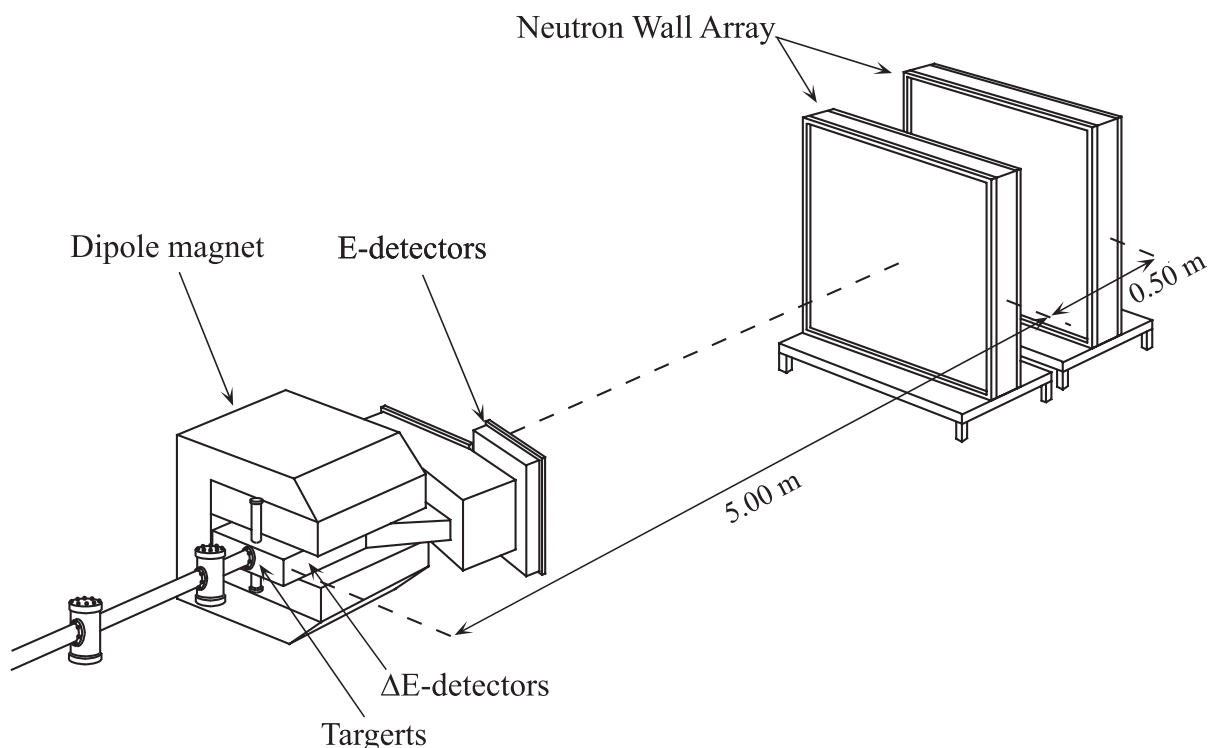


FIG. 2.—Layout of the experimental setup. The neutron walls, one behind the other, were placed 5.00 and 5.50 m from the target at  $0^\circ$ . The fragment detection system consists of silicon strip detectors ( $\Delta E$  detectors), the dipole magnet, and the plastic scintillator array ( $E$  detectors). The  $\Delta E$  detectors were located 15.2 cm downstream from the target at the entrance of the magnet.

gies and using a semiempirical formula that took into account the nonlinear response of the BC 408 (Fox et al. 1996), the light output was used to determine the energy of the  $^{14}\text{C}$  fragment in each dissociation event. Fragments having different rigidities hit different bars after being separated by the magnetic field. Furthermore, the  $\Delta E$ - $E$  technique of particle identification was used to help separate the two carbon isotopes.

The momentum vector of the neutron was determined in each event with the  $2 \times 2$  m NSCL neutron walls (Zecher et al. 1997) using the time-of-flight (TOF) technique. Each wall consists of 25 2 m long horizontal glass cells filled with NE 213 liquid scintillator; photomultiplier tubes are at both ends. As seen in Figure 2, the walls were at  $0^\circ$  and 5.00 and 5.50 m from the target. In the vertical direction the magnet aperture allowed only 1 m of the walls to be “seen” at the target, which limited the vertical acceptance to  $6^\circ 2'$ , while the horizontal length of the cells allowed a horizontal acceptance of  $11^\circ 6'$ . Three parameters were measured for each event: the light output, the horizontal position, and the time elapsed from the reaction in the target to the neutron hitting the wall. The resolutions ( $\sigma$ ) were 1.1 ns for time and 3 cm for position.

## 2.2. Data Analysis: Excitation Function for Dissociation Cross Section

To identify the relevant  $^{14}\text{C} + n$  coincidence events, we applied four conditions. (1) Neutron-induced pulses were separated from pulses induced by  $\gamma$ -rays by using a new pulse shape discrimination circuit (P. D. Zecher, D. Carter, & Z. Seres 2001, private communication). (2) The  $\Delta E$  signal was used to eliminate fragments having  $Z < 6$ . (3) To

reduce the number of in-scattered background neutrons, a time gate, indicated in the TOF spectra of Figure 3, was set on TOF corresponding to  $E_n = 15$ –53 MeV. This gate includes all neutrons from events with decay energy (see Fig. 1) less than  $\sim 1.5$  MeV, since backward- and forward-emitted neutrons of 1.5 MeV in the  $^{15}\text{C}$  rest frame have 15 and 53 MeV, respectively, in the laboratory. (4) In the  $E$ -detector pulse height spectra, the  $^{14}\text{C}$  and  $^{15}\text{C}$  peaks overlapped; therefore, we applied gates on the total energy spectra in individual bars and estimated the number of lost  $^{14}\text{C}$ 's for inclusion in the detection efficiency. A worst-case example for one of the scintillator bars is illustrated in Figure 4. The upper part shows the spectrum of fragment singles, which were counted simultaneously but downscaled by a factor of 1000. An overwhelming fraction of those events are unreacted  $^{15}\text{C}$ 's, but some may be  $^{14}\text{C}$ 's for which the neutron was not detected. When a neutron coincidence was required, we got the spectrum in the lower part. There, the  $^{14}\text{C}$ 's dominate, but extrapolations must be made to include  $^{14}\text{C}$ 's under the  $^{15}\text{C}$  peak and to exclude  $^{15}\text{C}$ 's under the  $^{14}\text{C}$  peak.

It is not possible to distinguish reactions producing coincidence events in a target from events produced in the silicon  $\Delta E$  detector. Therefore, in addition to running with each target in place, a sixth run was made with a blank target frame, and these events were subtracted from the events measured with each of the five targets. For the blank run, the beam energy was reduced by the average energy lost in the targets so that the energy of the beam striking the silicon was about the same as when the targets were in place.

For each  $^{14}\text{C} + n$  coincidence event, we transformed both velocity vectors to the CM system using Lorentz transfor-

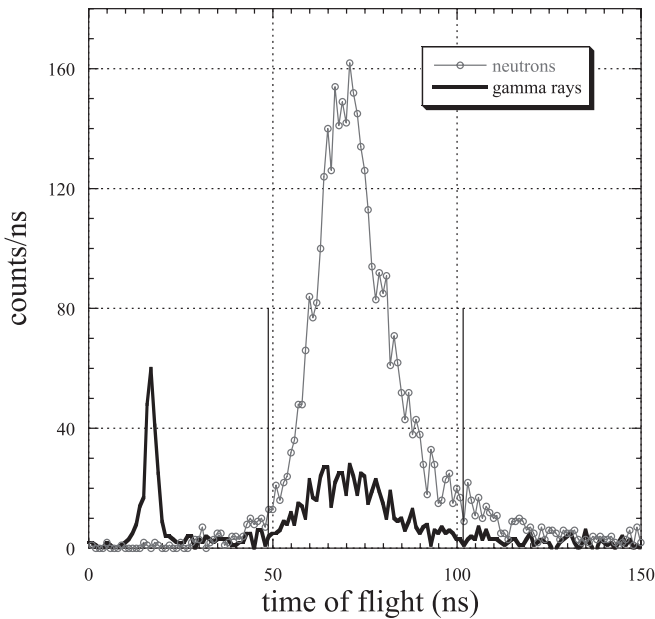


FIG. 3.—Neutron and  $\gamma$ -ray TOF spectra. The sharp peak at the left is from  $\gamma$ -rays produced in the target. The centroid of this peak served as a time reference for determining neutron energies. Only neutrons between channels 102 and 49, corresponding to  $E_n = 15$ –53 MeV, were used in the analysis.

mations, and the value of  $E_d$  was computed as  $\mu v_{\text{rel}}^2/2$ , where  $v_{\text{rel}}$  is the relative velocity in the CM system and  $\mu$  is the reduced mass of  $^{14}\text{C} + n$ . After dissociation, the velocity of the  $^{14}\text{C}$  fragment undergoes two changes before it can be measured. First, there is a Coulomb acceleration as it leaves the vicinity of the target nucleus, and then there is a deceleration by ionization energy loss as it traverses the remainder of the target. The two effects are in opposite directions. Since neither correction is knowable on an event-by-event basis, we made an average correction to the entire relative velocity distribution for each target.

To get absolute values of energy-dependent  $d\sigma/dE_d$  required a knowledge of efficiency and solid-angle acceptance of the neutron walls. The neutron detection efficiency was calculated with the code TOTEFF (R. J. Kurz 1964, Univ. California Report UCRL-11339) modified for NE213 (Doering 1974) using 1.6 MeVee (MeV electron equivalent) for the pulse height threshold. For the two neutron walls together, this efficiency was slightly energy-dependent, with an average of 22.1%. A curve of solid-angle acceptance times efficiency versus  $E_d$  was calculated by a simulation that took into account Rutherford deflection of the  $^{15}\text{C}$  before neutron emission, the geometrical layout of the system, and smaller effects such as multiple scattering in the target, the resolution of the  $n/\gamma$ -ray discrimination and the results of a shadow-bar analysis that corrected for neutron in-scattering. Graphs of  $d\sigma/dE_d$  for the five targets are shown by the points in Figure 5. Increasing statistical uncertainty caused us to cut off the presentation at 1200 keV.

Because of instrumental resolution widths, events with the same value of  $E_d$  will in general be experimentally determined to have a spread of values; that is, there is a detector response function that distorts the true shape of  $d\sigma/dE_d$  versus  $E_d$ . To find the true shape, a simulation was developed to calculate the detector response function. In this simula-

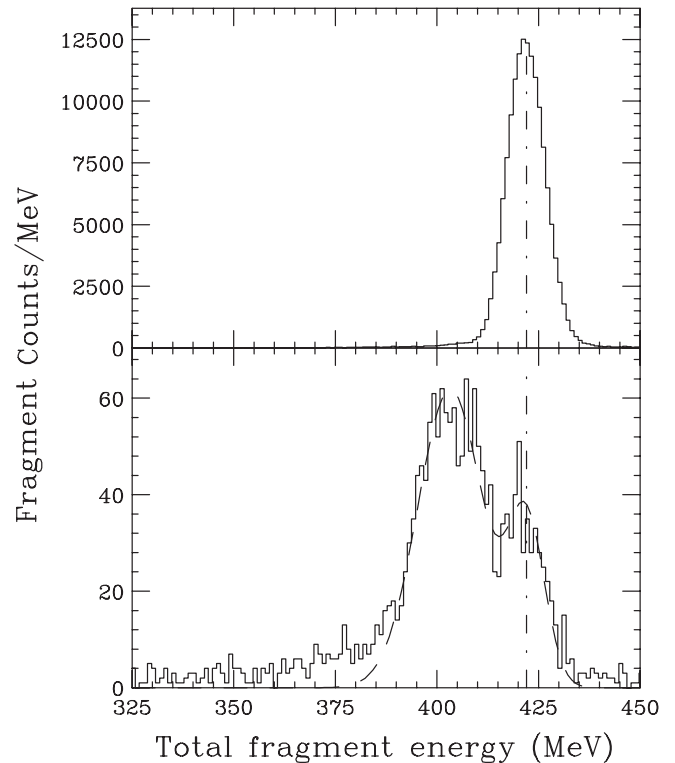


FIG. 4.—Spectra of fragments, singles above and coincident with neutrons below. A  $^{14}\text{C}$  peak that is invisible in the singles spectrum is dominant in the coincidence spectrum.

tion, all events actually had the same value of  $E_d$ , but random samplings of the errors in measuring the neutron TOF, the neutron angle, the  $^{14}\text{C}$  energy, and the  $^{14}\text{C}$  angle plus effects of the energy loss in the target, the Rutherford deflection, and the p-wave angular distribution of the emitted neutron produced a spread in  $E_d$ . The simulation treated its events in the same way as did the analysis of the real data. The simulation was performed every 20 keV in the range  $E_d = 20$ –1500 keV. Resolution functions for three values of  $E_d$  are shown in Figure 6.

As is usually the case, it is not possible here to use the measured  $d\sigma/dE_d$  and the response function to get the true  $d\sigma/dE_d$  in a direct manner. Instead, a trial-and-error method was used in which we guessed a true  $d\sigma/dE_d$ , folded in the response function, and compared the result with the data. Iterations produced a best fit, and  $d\sigma/dE_d$  for that fit was taken as the true  $d\sigma/dE_d$ . In detail, we note that the observed dissociation cross sections are described well by the empirical formula

$$\frac{d\sigma}{dE_d} = aE_d^p e^{-qE_d}, \quad (1)$$

where  $a$ ,  $p$ , and  $q$  are fitting parameters. The slope parameter  $q$  is determined by the decline of the higher energy part, the power parameter  $p$  is determined by the rising slope and the position of the maximum of the distribution, while the parameter  $a$  corresponds simply to the amplitude of the function. We used this shape as a trial function for the true  $d\sigma/dE_d$ , folded it with the resolution function, and made a least-squares fit to each set of data in Figure 5. These fits, which had  $\chi^2/d$  of less than 2.1 and  $p$  in a narrow interval

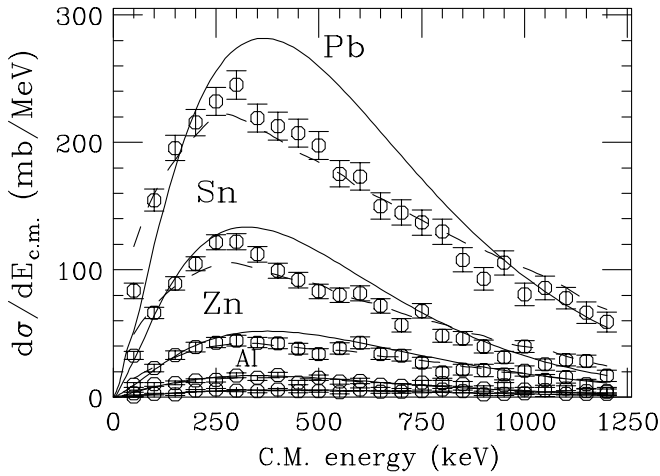


FIG. 5.—Dissociation excitation functions for C, Al, Zn, Sn, and Pb targets (C at bottom). Open circles are the data with statistical error bars. When the solid lines, the intrinsic (true) functions, are folded with the instrumental resolution functions of Fig. 6, the dashed-line fits result.

between 1.4 and 1.5, are given by the dashed lines. Functions in the form of equation (1) with the best-fit parameters are taken as the true  $d\sigma/dE_d$ ; they are given by the solid lines in Figure 5.

### 3. RESULTS: EXCITATION FUNCTION FOR NEUTRON CAPTURE CROSS SECTION

#### 3.1. Extraction of Coulomb Part of Dissociation Cross Section

Now that we have the true excitation functions for dissociation of  $^{15}\text{C}$ , we are ready to use those functions to extract that part that is Coulomb induced. The wide

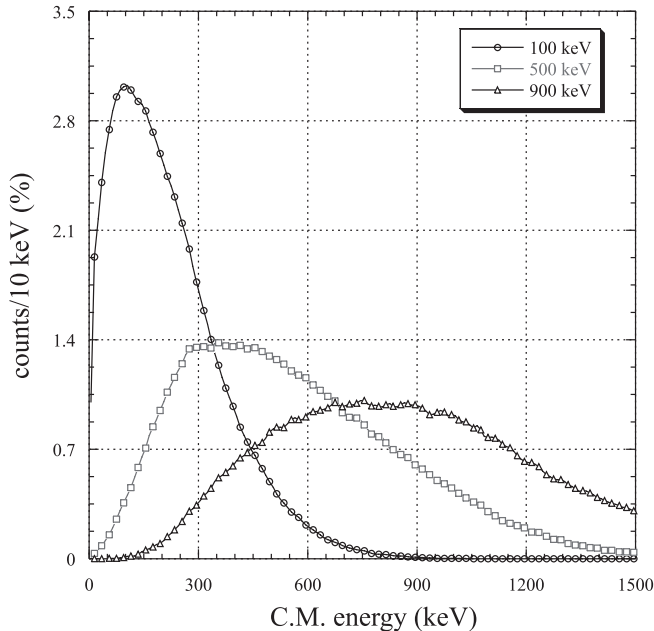


FIG. 6.—Resolution functions for the detector system at five different CM energies.

ranges of  $A$  and  $Z$  that characterize our targets make it easy to do this job, since nuclear and Coulomb processes have different dependences on these parameters. Since we observe both a neutron and a  $^{14}\text{C}$  in the forward direction, the reaction must proceed via a peripheral collision. The nuclear dissociation must, therefore, be proportional to  $2\pi r$ , and we take  $r$  to be the sum of the projectile and target radii. Coulomb dissociation, which depends on the spectrum of virtual photons associated with the nuclear charge, would simply be proportional to  $Z^2$  if the impact parameter had the same minimum value for each target. Because that value increases with  $A$  (and  $Z$ ), the exponent is less than 2 and is exactly calculable (Bertulani & Bauer 1988). Hence, we have

$$\frac{d\sigma}{dE_d}(E_d) = a(E_d)(r_0 A^{1/3} + r_{15c}) + b(E_d)Z^c. \quad (2)$$

For the radius parameters, we used  $r_0 = 1.2$  fm and  $r_{15c} = 2.96$  fm, and  $c$  varied from 1.87 to 1.80 for  $E_d = 0.05$ –1.2 MeV. Values for the left-hand side were taken from the solid curves of Figure 5. At each energy, we have five sets of known numbers,  $d\sigma/dE_d$ ,  $A$ , and  $Z$ , and by a least-squares fit  $a(E_d)$  and  $b(E_d)$  were determined. Representative fits and the Coulomb parts are shown in Figure 7 for three values of  $E_d$ . Nuclear dissociation dominates the reaction with carbon and aluminum targets and increases with energy, but at all energies the Coulomb part accounts for more than 95% of the dissociation with the Pb target, hence the Coulomb excitation function is within a few percent of the solid curve for Pb in Figure 5.

#### 3.2. $\sigma_{n,\gamma}(E_n)$ from $\sigma_{\gamma,n}(E_d)$

Although we have determined a photon-induced excitation function, it is not the excitation function for  $\sigma_{\gamma,n}$ , the inverse of  $\sigma_{n,\gamma}$ . The relation between  $\sigma_{\gamma,n}$  and the Coulomb part of  $d\sigma/dE_d$  is

$$\sigma_{\gamma,n}(E_\gamma) = \frac{E_\gamma}{n(E_\gamma)} \frac{d\sigma}{dE_d}(E_d) \Big|_{\text{Coul}}, \quad (3)$$

where  $E_\gamma = E_d + S_n$  (see Fig. 1) and  $n(E_\gamma)$  (Bertulani & Baur 1988) is the number function for virtual E1 photons.

The key part of our study is based on the principle of detailed balance. Since the neutron capture and its time-reversed process have the same matrix element, the two corresponding cross sections can be connected by the formula (Baur, Bertulani, & Rebel 1986)

$$\begin{aligned} \sigma_{n,\gamma}(E_{\text{CM}}) &= \frac{2(2j_{15c} + 1)}{(2j_{14c} + 1)(2j_n + 1)} \frac{k_\gamma^2}{k_{14c+n}^2} \sigma_{\gamma,n}(E_\gamma) \\ &= \frac{1}{\mu c^2} \frac{E_\gamma^2}{E_{\text{CM}}} \sigma_{\gamma,n}(E_\gamma), \end{aligned} \quad (4)$$

where  $\mu$  is the  $^{14}\text{C} + n$  reduced mass.

In a hot astrophysical environment, there may be a significant probability for the  $^{14}\text{C}$  nucleus to be in one of its excited states. The first excited state of  $^{14}\text{C}$  is at 6.1 MeV, which is well above the  $E_n = 0$ –1.2 MeV range of our experiment. Hence, there is no difference between laboratory and stellar capture cross sections.

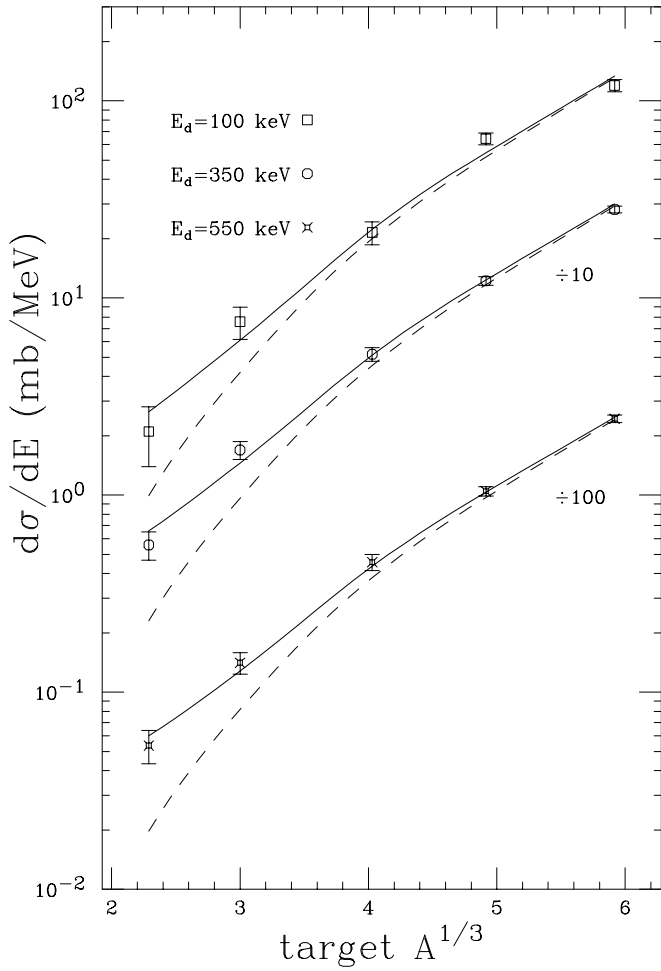


FIG. 7.—Total cross sections and Coulomb components of the dissociation at  $E_d = 100, 350,$  and  $550$  keV. Symbols are measured cross sections. Solid curves represent fits using eq. (2). Dashed curves are the Coulomb parts of the measured cross sections. The bottom two sets of points and fits have been displaced downward for clarity.

### 3.3. Correction for Branching Ratio

There is one complication. As was stated in the Introduction about the neutron capture process, “a p-wave neutron and  $^{14}\text{C}$  form  $1/2^-$  and  $3/2^-$  states, and the  $3/2^-$  states allow E1 transitions to both the ground and excited states.” Our measurement of an inverse reaction did not include the inverse of a transition to the excited state because our measurement always started with  $^{15}\text{C}$  in the ground state, never in the excited state. Fortunately, both the  $E_\gamma^3$  dependence of dipole transitions ( $[1.218/(1.218 - 0.740)]^3 = 16.5$  at  $E_d = 0$ ) and the measured spectroscopic factors (Goss et al. 1975;  $0.88/0.69 = 1.28$ ) favor the ground state. In addition, the  $1/2^-$  continuum states cannot make an E1 transition to the  $5/2^+$  excited state. The net result is an estimated correction to the measured part of  $\sigma_{n,\gamma}(E_n)$  that increases from 3% at  $E_n = 0$  to 16% at  $E_n = 1.2$  MeV.

### 3.4. The $^{14}\text{C}(n, \gamma)^{15}\text{C}$ Excitation Function

Including the enhancement for the unmeasured capture into the excited state of  $^{15}\text{C}$ , the left-hand side of equation (4) produced the diamond symbols in Figure 8. Experimentally allowed upper and lower limits, given by the two gray lines, were constructed from statistical uncertainties, from errors in applying the detector resolution function, and from errors in extracting the Coulomb part of the measured cross section.

The dashed curve is a prediction of Wiescher et al. (1990), and the dot-dashed curve is a prediction of Descouvemont (2000). The major differences between theory and experiment are the always higher theoretical values and the monotonically increasing theoretical curves in comparison to our experimental result, which peaks  $\sim 0.3$  MeV. Both of the calculations used a direct capture model that, due to the p-wave neutron penetrability, gave an initial energy dependence of  $E^{1/2}$ . Our initial energy dependence is consistent with  $E^{1/2}$ . Wave function simplifications in the calculations may account for their higher overall magnitudes, but we have no specific understanding of how such a large discrepancy could ensue. We have, of course, made all possible checks for experimental error.

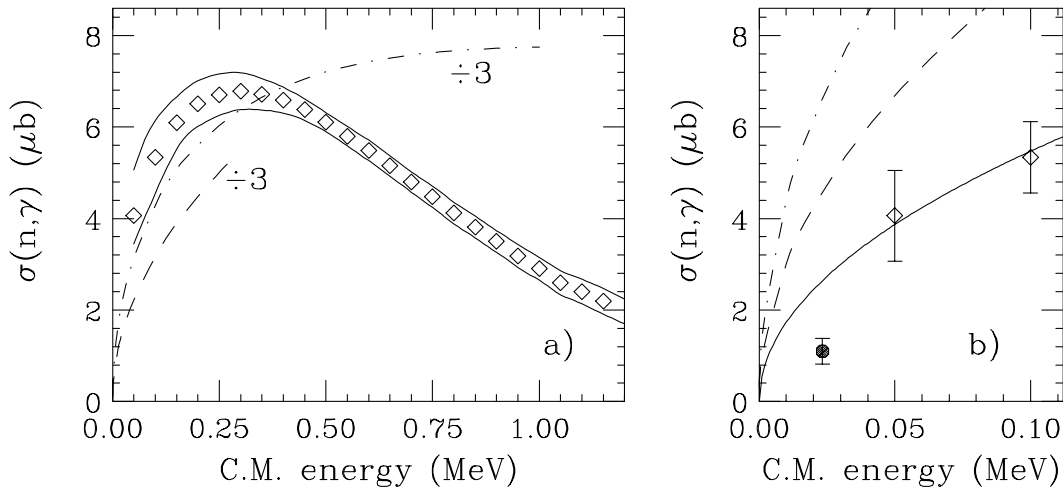


FIG. 8.—Excitation function for the  $^{14}\text{C}(n, \gamma)$  cross section. (a) Points enclosed by two solid curves define the region of the experimental results. Plotted as  $\frac{1}{3}$  of actual values, the dashed curve is a prediction of Wiescher et al. (1990), and the dot-dashed curve is a prediction of Descouvemont (2000). (b) Blowup of low-energy region showing same theoretical curves, but not divided by 3, the 1990 result of Beer et al. (solid point) and our lowest energy points (diamonds) with a kinematical fit (solid curve).

The only prior measurement (Beer et al. 1992) is represented by the point at 23 keV. It falls significantly below our experimental result and is even further from the prediction. In the blowup of the low-energy region on the right side of Figure 8, we have extrapolated to  $E = 0$  with a fit to our data whose energy dependence is that of  $T_{l=1}/E$  (Blatt & Weiskopf 1952). For very low energies, the centrifugal barrier transmission factor  $T_{l=1}$  for p-wave neutrons rises with  $E$  as  $E^{3/2}$ , giving the familiar  $E^{1/2}$  dependence of  $\sigma_{n,\gamma}$ , but as  $E$  increases,  $T_{l=1}$  rises more and more slowly than  $E^{3/2}$ , giving a  $\sigma_{n,\gamma}$  increase slower than  $E^{1/2}$ . (The deviation from an  $E^{1/2}$  dependence is less than 2% in Fig. 8b.) Our fit gives  $\sigma_{n,\gamma}(23 \text{ keV}) = 2.6 \pm 0.9 \mu\text{barns}$ , more than 2 times the result of Beer et al. (1992).

### 3.5. E2 Virtual Photons in the Dissociation Process

In principle, virtual photons of multipolarity other than E1 can contribute to  $^{15}\text{C}$  dissociation, in particular E2. In practice, however, E2 is strongly suppressed in comparison to E1 because of two factors. First, for multipolarity,  $\lambda$ , the effective charge,  $Z_{\text{eff}}^{(\lambda)} = Z_{14\text{C}} [m_n/(m_m + m_{14\text{C}})]^\lambda \cong Z_{14\text{C}} (1/15)^\lambda$ , which appears in the electric transition operator, reduces the ratio of E2/E1 transition probabilities by a factor of 225. In addition, Coulomb dissociation of  $^{15}\text{C}$  by an E2 photon requires the outgoing neutron to penetrate an  $l = 2$  centrifugal barrier, whereas E1 dissociation leads only to an  $l = 1$  barrier. Numerical calculations based on a model (Typel & Baur 2001) showed that the ratio of E2 to E1 dissociation is less than  $10^{-3}$  for  $E_d < 1.2 \text{ MeV}$ .

## 4. REACTION RATE

Since our measured excitation function in Figure 8 for the  $(n, \gamma)$  cross section differs from two theoretical predictions and from an earlier experimental result, the temperature dependencies of the corresponding reaction rates will also differ. The reaction rate is expressed in terms of the cross section by

$$R_{n,\gamma}(T) = N_A \langle \sigma v \rangle = N_A \left[ \frac{8}{\mu \pi (kT)^3} \right]^{1/2} \times \int \sigma_{n,\gamma}(E) E \exp\left(-\frac{E}{kT}\right) dE. \quad (5)$$

To evaluate this expression reliably up to temperature  $T$ ,  $\sigma_{n,\gamma}(E)$  should be known up to  $\sim E = 3kT$ . The energy limit of our measurement was 1.2 MeV. If we set  $3kT = 1.2 \text{ MeV}$ , the upper limit of the rate is  $T_9 \cong 5$ , where  $T_9$  is the temperature in units of  $10^9 \text{ K}$ . With an empirical formula to represent the results for  $\sigma_{n,\gamma}(E)$  and its error bounds in Figure 8, we performed the integral in equation (5) for  $T_9 = 0.1\text{--}5.0$  and obtained the rate functions shown by the solid curve and the enclosing gray curves in Figure 9. The curve corresponding to  $\sigma_{n,\gamma}(E)$  is described by the equation

$$R_{n,\gamma}(T) = \frac{2340 T_9}{(1 + T_9/6.18)^{5/2}}. \quad (6)$$

Corresponding to the theoretical  $\sigma_{n,\gamma}(E)$  of Descouvemont (2000), a similar formula was used to obtain the dot-dashed curve in Figure 9, and the upper dashed curve was plotted from the formula in Wiescher et al. (1990). These two theoretical rates are fairly close to each other, but, of course,

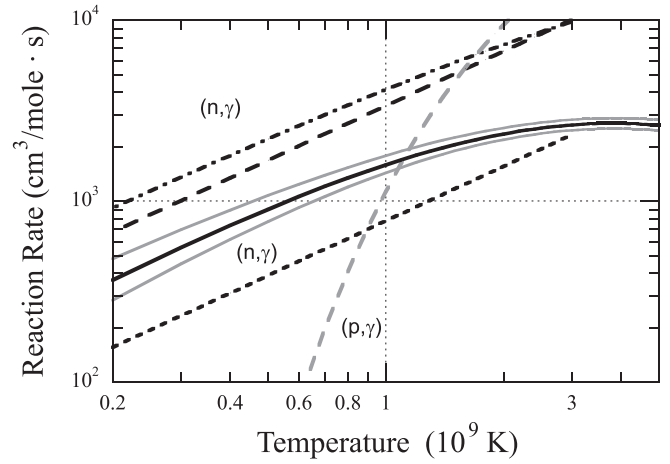


Fig. 9.—Reaction rates. Solid line enclosed by the gray error curves represents results of the present experiment. Dot-dashed curve (Descouvemont 2000), upper dashed curve (Wiescher et al. 1990), and the  $(p, \gamma)$  curve (Kawano et al. 1991) result from calculations. Dotted curve is derived from measured  $\sigma_{n,\gamma}$  at 23 keV by Beer et al. (1992).

they diverge from the experimental result as  $T$  increases. The dotted curve is derived from the measured point at 23 keV (Beer et al. 1992) with the same linear temperature dependence as in the upper dashed curve. At the low-temperature side of the figure, the helium-burning region, our results give greater importance to the  $^{14}\text{C}(n, \gamma)$  reaction than was previously demonstrated.

The rate of proton capture on  $^{14}\text{C}$  (Kawano et al. 1991) is also plotted in Figure 9. Its temperature dependence is much stronger than the temperature dependence of the neutron capture reaction, and the proton curve intersects all four of the neutron curves, but at rather different temperatures. In the temperature range important for inhomogeneous big bang models,  $T_9 = 0.2\text{--}1.2$ , the point of intersection determines the relative importance of the two reactions,  $^{14}\text{C}(p, \gamma)^{15}\text{N}$  and  $^{14}\text{C}(n, \gamma)^{15}\text{C}$ . In Figure 9, we see that this point varies from  $T_9 = 0.9$  to 1.7.

## 5. SUMMARY AND CONCLUSIONS

In an inhomogeneous early universe, nucleosynthesis in neutron-rich regions could produce observable amounts of  $A > 12$  isotopes, whereas the standard big bang nucleosynthesis ends with  $^7\text{Li}$ . Once we reach  $^{12}\text{C}$ , the path for production of  $A > 20$  elements depends, among other things, on the cross section for neutron capture on  $^{14}\text{C}$ .

By performing an experiment on dissociation of  $^{15}\text{C}$  into  $^{14}\text{C} + n$  with projectiles of  $^{15}\text{C}$  on targets of C, Al, Zn, Sn, and Pb, we were able to extract the Coulomb part of the dissociation cross section. This was equivalent to measuring the cross section for the  $^{15}\text{C}(\gamma, n)^{14}\text{C}$  reaction, the inverse of the  $^{14}\text{C}(n, \gamma)^{15}\text{C}$  reaction. By applying the principle of detailed balance, we determined the cross section for the  $^{14}\text{C}(n, \gamma)^{15}\text{C}$  reaction. In comparison to the only previous measurement, one at 23 keV, our result is higher by a factor of 3. This increases the importance of the  $^{14}\text{C}(n, \gamma)^{15}\text{C}$  reaction at helium-burning temperatures. The inverse technique enabled us to measure the cross section up to  $E_n \sim 1.2 \text{ MeV}$ . In comparison to theoretical predictions, the experimental excitation function is generally lower and has a different

energy dependence. Theory and experiment both rise quickly at low energies, but above 100 keV the experimental result differs significantly from the  $E^{1/2}$  function of the predictions, and from 0.2 to 1.2 MeV it falls by a factor of 3. From our measured excitation function for the  $^{14}\text{C}(n, \gamma)^{15}\text{C}$  reaction we determined its reaction rate up to a temperature of  $5 \times 10^9$  K. After an initial linear rise with temperature, it appears to be leveling off at  $T_9 = 5$ , whereas the theoretical reaction rates continue to rise with temperature. In the temperature range of inhomogeneous big bang models our rate exceeds the rate of the  $^{14}\text{C}(p, \gamma)^{15}\text{N}$  reaction for  $T_9 < 1.2$ .

We thank Don Sackett for proposing the experiment, Thomas Rauscher and Hendrik Schatz for helpful comments after reading drafts of this paper, and Pierre Descouvemont for sending us his results for inclusion in Figure 8. This material is based on work supported by the National Science Foundation under grants PHY-9528844, PHY-9423659, and PHY-9901133, OTKA T032113 of the Hungarian Science Foundation, the Bolyai Research Foundation, the Ministry of Education, Science, Sports, and Culture of Japan, and the Japan Society for the Promotion of Science.

## REFERENCES

- Alder, K., & Winther, A. 1966, *Coulomb Excitation* (New York: Academic)
- Baur, G., Bertulani, C. A., & Rebel, H. 1986, *Nucl. Phys. A*, 458, 1886
- Beer, H., Wiescher, M., Käppeler, F., Görres, J., & Koehler, P. E. 1992, *ApJ*, 387, 258
- Bertulani, C. A., & Baur, G. 1988, *Phys. Rep.*, 163, 302
- Blatt, J. M., & Weiskopf, V. F. 1952, *Theoretical Nuclear Physics* (New York: Wiley)
- de Bernardis, P., et al. 2000, *Nature*, 404, 955
- Descouvemont, P. 2000, *Nucl. Phys. A*, 675, 559
- Doering, R. R. 1974, Ph.D. thesis, Michigan State Univ.
- Fox, D., Bowman, D. R., Ball, G. C., Galindo-Urbarri, A., Hagberg, E., Horn, D., Beaulieu, L., & Larochelle, Y. 1996, *Nucl. Instrum. Methods Phys. Res. A*, 374, 63
- Goss, J. D., Jolivet, P. L., Browne, C. P., Darden, S. E., Weller, H. R., & Blue, R. A. 1975, *Phys. Rev. C*, 12, 1730
- Hanany, S. et al. 2000, *ApJ*, 545, L5
- Jedamzik, K., & Rehm, J. B. 2001, *Phys. Rev. D*, 64, 023510
- Kainulainen, K., Kurki-Suonio, H., & Sihvola, E. 1999, *Phys. Rev. D*, 59, 083505
- Kainulainen, K., & Sihvola, E. 2001, *Phys. Rev. D*, 63, 083508
- Kajino, T., Matthews, G. J., & Fuller, G. M. 1990, *ApJ*, 364, 7
- Kawano, L. H., Fowler, W. A., Kavanagh, R. W., & Malaney, R. A. 1991, *ApJ*, 372, 1
- Kruse, J. J., Galonsky, A., Snow, C., Tryggestad, E., Wang, J., Ieki, K., Iwata, Y., & Zecher, P. D. 2002, *Nucl. Instrum. Methods Phys. Res. A*, 480, 598
- Malaney, R. A., & Fowler, W. F. 1988, in *The Origin and Distribution of the Elements*, ed. G. J. Matthews (Singapore: World Scientific), 76
- Orito, M., Kajino, T., Boyd, R. N., & Mathews, G. J. 1997, *ApJ*, 488, 515
- Rauscher, T., Applegate, J. H., Cowan, J. J., Thielemann, F. K., & Wiescher, M. 1994, *ApJ*, 429, 499
- Sherrill, B. M., Morrissey, D. J., Nolen, J. A., & Winger, J. 1991, *Nucl. Instrum. Methods Phys. Res. B*, 56, 1106
- Typel, S., & Baur, G. 2001, *Phys. Rev. C*, 64, 024601
- Wiescher, M., Görres, J., & Schatz, H. 1999, *J. Phys. G: Nucl. Part. Phys.*, 25, R1
- Wiescher, M., Görres, J., & Thielemann, F. K. 1990, *ApJ*, 363, 340
- Yaffe, L., & Stevens, W. H. 1950, *Phys. Rev.*, 79, 893
- Zecher, P. D., et al. 1997, *Nucl. Instrum. Methods Phys. Res. A*, 401, 329